Divergence Compensatory Optical Flow Method for Blood Velocimetry

Zifeng Yang[1]
Department of Mechanical and Materials Engineering
Wright State University
3640 Colonel Glenn Hwy
Dayton, OH 45435
E-mail: zifeng.yang@wright.edu

Hongtao Yu
Department of Mechanical and Materials Engineering
Wright State University, Dayton, OH 45435
E-mail: yu.41@wright.edu

George P. Huang
Department of Mechanical and Materials Engineering
Wright State University, Dayton, OH 45435
E-mail: george.huang@wright.edu
ASME Fellow

Bryan Ludwig
Wright State University Boonshoft School of Medicine
Wright State University, Dayton, OH 45435
Department of Neurology – Division of NeuroInterventional Surgery
Wright State University / Premier Health - Clinical Neuroscience Institute
30 E. Apple St, Dayton OH 45409
Email: brludwig@PremierHealth.com

[1] Corresponding author

ABSTRACT

Detailed blood velocity map in vascular system can be obtained by applying the optical flow method (OFM) in processing fluoroscopic digital subtracted catheter angiographic images, however, there are still challenges with the accuracy of this method. In the present study, a divergence compensatory Optical Flow Method (DC-OFM), in which a non-zero divergence of velocity is assumed due to the finite resolution of the image, was explored and applied to the digital subtraction angiography (DSA) images of blood flow. The objective of this study is to examine the applicability and evaluate the accuracy of DC-OFM in assessing the blood flow velocity in vessels. First, an Oseen vortex flow was simulated on the standard particle image to generate an image pair. Then, the DC-OFM was applied on the particle image pair to recover the velocity field for validation. Second, DSA images of intracranial arteries were used to examine the accuracy of the current method. For each set of images, the first image is the in vivo DSA image, and the second image is generated by superimposing a given flow field. The recovered velocity map by DC-OFM agrees well with the exact velocity for both the particle images and the angiographic images. In comparison with the traditional OFM, the present method can provide more accurate velocity estimation. The accuracy of the velocity estimation can also be improved by implementing pre-process techniques including image intensification, Gaussian filtering and "image -shift".

Keywords: Optical Flow Method, Blood velocity, Velocimetry

INTRODUCTION

Diseases in the vascular system are still the leading cause of mortality and morbidity in developed countries despite considerable therapeutic progress in recent years [1-3]. Blood velocity information has been recognized as useful, significant or even critical data for monitoring of endovascular treatment of brain arteriovenous malformations and aneurysms, diagnosis of vascular diseases and radiosurgery treatment planning [1]. Recently, wall shear

stress (WSS) [4-6] and mean aneurysm flow amplitude (MAFA) [7] have been suggested by various research groups as indicators for diagnosis of vascular disease, treatment planning, and risk assessments. To assess these indicators, detailed velocity distributions from *in vivo* experiments are needed.

The routine diagnostic techniques for *in vivo* blood flow visualization include; ultrasound sonography, magnetic resonance imaging (MRI), computed X-ray tomography (CT), and x-ray angiography. These techniques can provide some *in vivo* flow information which has been used for diagnosis of vascular disease. However, MRI suffers from poor signal-to-noise ratios and the temporal and spatial resolution is not adequate for small-scale endovascular flow such as some small-scale cerebrovascular flows. CT does not provide any blood velocity information due to the method of acquisition. The penetration depth and accuracy for ultrasound sonography is limited. For the reasons outlined above, X-ray angiography is the ideal form of medical imaging for Optical Flow Method (OFM) calculations [3]. In X-ray angiography, the radio-opaque contrast agent (usually iodine-based) causes the darkness pattern shown in the X-ray image. For high-quality imaging of cerebral and cardiac blood vessels, digital subtraction angiography (DSA), in which a pre-contrast image is subtracted from the latter images, has its unique advantage in terms of resolution and accuracy. *In vivo* blood flow velocity measurements can be achieved from the movement of the contrast agent which shows a texture pattern in X-ray angiograms. Roentgen-videodensitometric blood velocity quantification based on digital x-ray angiograms is recognized as a well-published research topic [8]. The currently adopted methods, such as simplified OFM and continuity-based method, are widely accepted for producing velocity distribution for clinical needs and computational validation [8].

The optical flow method, which was originally proposed to capture visual motion in digital pictures by Horn and Schunck [9], has been further developed for fluid flow measurements [10-13]. In principle, the OFM is based on the assumption that the brightness of a particular point in the image pattern is constant, and a differential-equation algorithm is suitable for calculation of small displacement vectors (one velocity vector per pixel) by comparing two consecutive images with continuous patterns of the flow field. With the smoothness constraint applied to the intensity distribution, the corresponding Euler-Lagrange equation can be derived and solved to obtain the two-dimensional (2D) velocity field. The algorithm is explained in the following section. Early efforts focused on using the OFM on DSA by estimating one-dimensional velocity and/or gross mass flow rate using the simplified optical flow method [14-16]. An injection of contrast material is introduced into the blood stream, and the contrast is then diluted and modulated by the cardiac cycle through the vascular network. The resulting contrast wave propagates through the arterial lumen and thus moving patterns are created and so called “optical flow.” The optical flow is transferred to the 2D velocity field using the Horn and Schunck’s optical flow algorithm [17, 18]. Pereira et al. [19] applied the OFM on the quantification of internal carotid artery flow with DSA, in which the OFM results were roughly compared with Doppler ultrasound measurements. They identified two key factors: (1) a short time interval between consequential images, and (2) flat panel technology in order to make the image compatible with the optical flow algorithm [19]. Two-dimensional velocity distribution could be obtained; however, the comparison was only conducted in terms of volume flow rate or streamlines. Detailed quantitative validation in a 2D fashion (i.e., vector by

vector validation) is still not available. For the analysis of WSS and MAFA, accurate high-resolution velocity distributions are essential.

Recently, the quantitative connection between the optical flow and fluid flow was established by Liu and Shen [20] through the projection of the transport equations in the physical space onto the image plane. They also obtained a physics-based optical flow equation in which the optical flow was defined as the path-averaged velocity of fluid (or particles). This provides a rational foundation for application of the OFM to various flow visualization images. It has been proved that more accurate velocity estimation can be produced by applying physics-based OFM on flow images generated from various visualization techniques [20].

The physics-based OFM has not been applied and validated toward X-ray images of endovascular flow, which is more challenging because of limitations of validation techniques for 2D/3D measurements in the *in-vivo* environment. Based on the physics-based OFM, a divergence compensatory optical flow method (DC-OFM) is developed to estimate flow velocity from X-ray images. The physical obstacles for *in vivo* experiment include the selections of tracer particles, illumination difficulties, and duration of X-ray exposure. Therefore, in this study, we used image pairs, in which the first image is extracted from the original X-ray angiography, and the second image is generated by simulating a known flow field on the first image. This allowed us to study the accuracy of the DC-OFM in calculating the velocity field. The objective of the present study is to examine the capability of the DC-OFM in dealing with the X-ray images and evaluate the accuracy of the DC-OFM in detail (i.e., pixel by pixel) with the end goal to produce the velocity map of blood flow in human vasculatures. In order to examine the algorithm systematically and conduct the error analysis, Oseen vortex flow simulations were conducted

on a random particle image to generate the high-quality image pair for the OFM analysis. Finally, the DC-OFM algorithm was applied to the DSA image pairs of intracranial arteries, including both the internal carotid artery (ICA) and the cerebral aneurysm, in which the first image is cropped from the original DSA image, and the second image is a synthetic image that is generated by superimposing the Computational Fluid Dynamics (CFD) simulation velocity field based on the same geometry.

2. Methodology

2.1 Optical Flow Method

The relation between fluid flow and optical flow were discussed in detail by Liu and Shen [20]. The projected motion equations for several typical flow visualizations were carefully derived as that the optical flow velocity $\vec{v}$ is proportional to the path-averaged displacement of particles in the physical flow field. The physics-based optical flow algorithm was obtained by taking into consideration of the physical boundary, diffusion effect, and accumulation effect in the control volume [20], as follows

$$\frac{\partial E}{\partial t} + \nabla \cdot (E\vec{v}) = f(x, y, E), \tag{1}$$

where E represents the intensity in the image, $\vec{v}$ is the velocity vector, and the source term

$$f(x, y, E) = D\nabla^2 E + Dc_f B + c_f \vec{n} \cdot \left(\psi \vec{V}|_{\Gamma_1}^{\Gamma_2}\right). \tag{2}$$

where $D\nabla^2 E$ accounts for the diffusion motion of the contrast material in blood flow, D is the diffusion coefficient, B represents the boundary term which is in relation to the quantity

ψ, which is a scalar in flows (e.g. dye), over the control surface, c_f is a scattering/absorption coefficient for particles or fluorescence, and $\vec{n} \cdot (\psi \vec{v}|_{\Gamma_1}^{\Gamma_2})$ represents the accumulation effect of the field quantity ψ, $\Gamma_{1,2}$ represents the control surface in the out-of-plane direction [20].

Compared with the brightness constraint equation given by Horn and Schunck [9],

$$\frac{\partial E}{\partial t} + \vec{v} \cdot \nabla E = 0, \tag{3}$$

Equation (1) contains two more terms, $E\nabla \cdot \vec{v}$, and f, which represents the divergence effect in continuity and source of intensity change within the control volume, respectively. Equation (1) can be re-written as

$$\frac{\partial E}{\partial t} + \vec{v} \cdot \nabla E + E\nabla \cdot \vec{v} = D\nabla^2 E + Dc_f B + c_f \vec{n} \cdot \left(\psi \vec{v}|_{\Gamma_1}^{\Gamma_2}\right). \tag{4}$$

From a theoretical analysis, the transmittance of X-ray light through the body area of interest can remain constant within an extremely short time interval. Therefore the boundary term B can be neglected for the current algorithm. The "accumulation effect" of the illuminance is considered as negligible, i.e., $c_f \vec{n} \cdot \left(\psi \vec{v}|_{\Gamma_1}^{\Gamma_2}\right) \approx 0$. Ideally, if the angiographic imaging is acquired after the contrast agent is all injected, a conservation of image intensity within a short time interval can be assumed. However, in the practical X-ray angiography process, images were always obtained while the contrast injection is in process. In order to make the conservation assumption valid, an extremely short time interval is required which will need to be verified through future experiments. The diffusion effect should be taken into account although the absolute value is relatively small. Ultimately, the physics-based optical flow equation used in the current proposed method is

$$\frac{\partial E}{\partial t} + \vec{v} \cdot \nabla E + E\nabla \cdot \vec{v} = D\nabla^2 E. \quad (5)$$

In this equation, the term $\frac{\partial E}{\partial t} + \vec{v} \cdot \nabla E$ represents brightness constancy which was used in the traditional OFM, while the term $E\nabla \cdot \vec{v}$ accounts for the non-conservation of the brightness function due to non-zero out of plane movement and divergence residual due to finite resolution. The term $D\nabla^2 E$ accounts for the diffusion effect of the contrast agent in the flow. These two accounts for the improvement of the OFM method toward a more accurate velocity estimation.

2.2 Variational formulation

To solve the optical flow equation, a variational formulation with a smoothness constraint was proposed by Horn and Schunck [9]. Due to its simplicity, Horn and Schunck's constraint is adopted. The function to be minimized is defined as

$$J(\vec{v}) = \int_A [\frac{\partial E}{\partial t} + \nabla \cdot (E\vec{v}) - f]^2 dxdy + \alpha \int_A (|\nabla u|^2 + |\nabla v|^2)\, dxdy, \quad (6)$$

where α is the Lagrange multiplier. To minimize $J(\vec{v})$, The gradient $\nabla J(\vec{v})$ will be defined by $dJ(\vec{v} + \varepsilon\vec{w})/d\varepsilon|_{\varepsilon=0}$, where $\vec{w}$ is an arbitrary function that prescribes the "direction" in which the derivative is computed.

Using the calculus of variation, the general Euler-Lagrange equation can be obtained by

$$\frac{\partial L}{\partial \vec{v}} - \frac{d}{d\vec{x}}\frac{\partial L}{\partial \vec{v}'} = 0, \quad (7)$$

where L is the integrand equation in Equation (6), $\vec{v}'$ is the derivative of velocity. For the current two-dimensional problem, this equation can be divided into two equations as

$$\frac{\partial L}{\partial u} - \frac{\partial}{\partial x}\frac{\partial L}{\partial u_x} - \frac{\partial}{\partial y}\frac{\partial L}{\partial u_y} = 0 \tag{8}$$

$$\frac{\partial L}{\partial v} - \frac{\partial}{\partial x}\frac{\partial L}{\partial v_x} - \frac{\partial}{\partial y}\frac{\partial L}{\partial v_y} = 0 \tag{9}$$

where $L = [\frac{\partial E}{\partial t} + \nabla \cdot (E\vec{v}) - f]^2 + \alpha(|\nabla u|^2 + |\nabla v|^2), u_x, u_y, v_x$, and v_y are spatial derivatives of velocities. Through combining terms in these two equations, with $f = D\nabla^2 E$, the corresponding vector-version Euler-Lagrange equation can be obtained as

$$E\nabla[\partial E/\partial t + \vec{v} \cdot \nabla E + E\nabla \cdot \vec{v} - D\nabla^2 E] + \alpha\nabla^2\vec{v} = 0, \tag{10}$$

where α is the Lagrange multiplier. By expanding the equation (7), it can be expressed in scalar component equations relative to an *x*-*y* coordinate system,

$$E\frac{\partial^2 E}{\partial t \partial x} + E\frac{\partial E}{\partial y}\frac{\partial v}{\partial x} + E\frac{\partial E}{\partial x}\frac{\partial u}{\partial x} + uE\frac{\partial^2 E}{\partial x^2} + vE\frac{\partial^2 E}{\partial y^2} + E^2\frac{\partial^2 u}{\partial x^2} + E^2\frac{\partial^2 v}{\partial x \partial y} + E\frac{\partial E}{\partial x}\frac{\partial u}{\partial x} + E\frac{\partial E}{\partial x}\frac{\partial v}{\partial y}$$

$$-DE\frac{\partial^3 E}{\partial x^3} - DE\frac{\partial^3 E}{\partial y^2 \partial x} + \alpha\frac{\partial^2 u}{\partial x^2} + \alpha\frac{\partial^2 u}{\partial y^2} = 0, \tag{11}$$

$$E\frac{\partial^2 E}{\partial t \partial y} + E\frac{\partial E}{\partial x}\frac{\partial u}{\partial y} + E\frac{\partial E}{\partial y}\frac{\partial v}{\partial y} + uE\frac{\partial^2 E}{\partial x \partial y} + vE\frac{\partial^2 E}{\partial y^2} + E^2\frac{\partial^2 v}{\partial y^2} + E^2\frac{\partial^2 u}{\partial x \partial y} + E\frac{\partial E}{\partial y}\frac{\partial u}{\partial x} + E\frac{\partial E}{\partial y}\frac{\partial v}{\partial y}$$

$$-DE\frac{\partial^3 E}{\partial x^2 \partial y} - DE\frac{\partial^3 E}{\partial y^3} + \alpha\frac{\partial^2 v}{\partial x^2} + \alpha\frac{\partial^2 v}{\partial y^2} = 0. \tag{12}$$

A 5-point based second-order discrete scheme, as suggested by Liu and Shen [20], has been adopted and applied to Equations (8) and (9) in the current study to solve the velocity numerically. The linear system is solved by using Jacobi's blockwise iteration method [20]. The iteration process is ended when the remaining error reaches a predetermined small value. Note that in the present study, diffusion effect was not simulated in generating the second image by superimposing a known flow field. Therefore, diffusion coefficient D was set as zero in the

present application. In the current flow solver, Horn-Schunck method was applied to the image pair to obtain a rough velocity field due to its simplicity. Then this estimation result serves as the initial velocity input for the present OFM, which can accelerate the convergence process.

2.3 Error analysis

In the optical flow algorithm, image intensity is the sole input while the output is the velocity distribution. In the process of image acquisition, all measurement noise was included which could cause errors in the velocity estimation. There is also a resolution-based error and truncation error because the image is usually saved as 8-bits image with finite resolution. The image intensity and velocity can be decomposed into an exact value and an error component:

$$E = E_{exact} + \Delta E, \tag{13}$$

$$\vec{v} = \vec{v}_{exact} + \Delta\vec{v}. \tag{14}$$

Substituting Equations (13) and (14) into Equation (10), neglecting small terms of higher order and with the assumption of exchangeability between the difference (Δ) and del operator (∇), the error propagation equation is obtained as

$$E\nabla\left[\Delta\left(\frac{\partial E}{\partial t}\right) + \Delta(\nabla E)\cdot\vec{v} + E\Delta(\nabla\cdot\vec{v}) + \Delta E(\nabla\cdot\vec{v}) + \nabla E\cdot(\Delta\vec{v})\right] + \alpha\nabla^2(\Delta\vec{v}) = \alpha(\Delta E/E)\nabla^2(\vec{v}). \tag{15}$$

The elemental error sources are $\Delta(\partial E/\partial t)$, $\Delta(\nabla E)$, $\Delta(\nabla\cdot\vec{v})$, and ΔE. Among these terms, $\Delta(\partial E/\partial t)$, $\Delta(\nabla E)$ are the numerical errors associated with the temporal and spatial derivatives of the image intensity value, respectively. $\Delta(\nabla\cdot\vec{v})$ is the error in the divergence of the flow velocity. Moreover, the error in the final velocity calculation is also dependent on the image intensity gradient ∇E and the Lagrange multiplier α.

For a limiting case in which elemental errors $\Delta(\nabla E)$, $\Delta(\nabla \cdot \vec{v})$ and ΔE can be considered as negligible, the optical flow error $\Delta\vec{v}$ is then mainly caused by $\Delta(\partial E/\partial t)$. We are interested in this case because the requirement of a short time interval and high intensity gradient is particularly challenging using DSA images in the present study. Liu and Shen [20] pointed that for a given value of Δt, a larger intensity gradient contribute less error in the optical flow. For images with a large intensity gradient, the need for a short Δt can be relaxed. Conversely, if the gradient is low, a relatively smaller Δt is critical to improve the accuracy of the optical flow algorithm.

2.4 Acquisition of DSA images

3D rotational angiography is ubiquitously utilized in vascular diseases visualization. As the contrast medium injected in the arteries will created blockage of the x-ray and hence generate a relatively low-brightness region in the image. The random distribution of the contrast agent diluted in the blood stream will create a brightness pattern in the angiographic images, as presented in Fig. 1. The intracranial vasculatures with an internal carotid artery (ICA) aneurysm were visualized by 3D rotational angiography (Siemens Artis Zee) from a female patient (64 year old, Caucasian, with no smoking history or family history of RIAs). The sequence images were acquired with an acquisition rate of 6 Hz. During the image acquisition, the ICA was careful catheterized using a 5F Terumo angle taper catheter. A power injector connected to the catheter injects 3 ml s^{-1} of contrast in average (Visipaque 300). 30 images were acquired during a 5 second spin of the imaging arm with a variable rate of contrast injection depending on the patient's cardiac output and prior contrast injection. The image is then stored in DICOM format and de-identified by the operating physician. In the present study, a single slice image was used to examine the optical flow method therefore only a two-

dimensional flow field can be obtained. Fig.1 presents the DSA image of the cerebral vasculature and a cropped image focusing on merely a section of ICA for the present study.

2.4 Generation of image pair and image processing techniques

2.4.1 Particle images

In order to validate the present optical flow algorithm and explore the factors determining the accuracy of the velocity estimation, first, the present algorithm is applied to the random particle images. At the current stage, even though the particle images are fundamentally different from the DSA images, they are still selected for validation and parameter study purposes, as particle images have been widely accepted for validation of image velocimetry algorithms [20, 21]. On the other hand, tiny particles (CO_2 microbubbles) have been proposed for X-ray PIV measurement of blood flow as well [22], which could generate particle images of blood flow. As discussed in the error analysis, the local intensity gradient and time interval are key parameters affecting the velocity accuracy. These two key parameters will be studied using the particle images as well. The first particle image (256 pixel × 256 pixel) is adopted from a previous work by Okamoto et al. [23]. In order to satisfy the smooth constraint for the OFM, a Gaussian filter (mask size, s, of 3×3 pixel and standard deviation, σ, of 1.2 pixels) is implemented twice in filtering the image to generate a blurred image with smooth pattern. A synthetic flow field is simulated by superimposing an Oseen vortex pair into a uniform flow as introduced in the study of Liu and Shen [20]. The two Oseen vortices are placed at (x = 128 pixels, y = 85 pixels) and (x = 128 pixels, y = 170 pixels)

respectively in the image. The velocity magnitude along circumferential direction generated by the Oseen vortex is given by

$$u_\theta = (\omega/2\pi r)[1 - \exp(-r^2/r_c^2)], \quad (16)$$

where the core radius r_c is set as 15 pixels, and the vortex strength ω is set as ± 3000 (pixel)^2 s^{-1} depending on the position. The uniform flow velocity is set as 10 pixel s^{-1} towards right in the image. The second particle image was generated shifting all particles by superimposing the given flow field by Equation (16) with a time step Δt governed by the Equation (5) with $D = 0$. These parameters are selected with an appropriate time step for the purpose of generating a maximum velocity magnitude of 0.5 pixel frame^{-1}, which results in the best accuracy for the current optical flow method.

2.4.2 DSA images

The present study intends to apply the DC-optical flow in processing the DSA images of blood flow in vasculature to obtain the close-real-life blood velocity distribution. To validate the current method, the accurate flow velocity data is needed for comparison. However, there is no technique available *in vivo* to provide a detailed accurate blood velocity measurement for the validation purpose. Therefore, we employ the computational fluid dynamic (CFD) tool to simulate the flow field using the blood vessel geometry extracted from the DSA image. The objective for CFD simulation is merely to provide a reasonable velocity distribution to generate the synthetic image. Therefore, the accuracy of the CFD simulation is not a concern in the present work. Then the velocity distribution is superimposed into the original DSA image to generate the second image as described above. The produced velocity field from the present OFM can be compared with the given velocity distribution from CFD.

To simplify the CFD simulation, only a part of the arteries shown in Fig. 1 (a) was cropped from the original image. The CFD calculation approach for simulations of flow in the vasculature was adopted from a commercial CFD software *SC/Tetra* (Cradle North America, Dayton, OH). The *SC/Tetra solver* utilizes a finite volume method to solve the governing equations containing continuity and momentum equations. The 2D configuration boundary was generated through extracting the blood vessel from the image, and was used to generate the mesh in *SC/Tetra* for the CFD simulation. As Reynolds number for this type of flow is very low (less than 2000), six layers of structured mesh (rectangle) was implanted at the wall boundary. Other regions in the lumen were meshed using unstructured mesh (triangle). A rigid wall boundary condition was adopted for a flow rate of 1 (dimensionless), and pressure at the exit is set as 0. It is noted that in the case of aneurysm study, a phantom artery was added because the outlet artery in the original image was not visible, as present in Fig. 2. To enable the CFD simulation, the parent phantom artery is added in the CFD modelling to generate a reasonable flow in the aneurysm (having both inlet and outlet). For this case, only the flow distribution in the aneurysm will be used to generate the image pair, as long as the flow in the aneurysm satisfies the rigid wall boundary condition, which is considered as a reasonable flow, the flow in the phantom artery is not a concern for the present study. Therefore the selection of the phantom parent artery is arbitrary.

According to the conclusion from Liu and Shen [20], in general, a greater intensity gradient is more in favor of OFM. It can be observed that the DSA image of blood flow should be characterized as isotropic distribution of intensity, which results in a low intensity gradient. Therefore, the DSA image is further cropped to only leave the blood flow region for further

image processing. For the purpose of enhancing the intensity gradient, the original image was intensified by multiplying the intensity value for each pixel by a factor, $\beta = 2.0$ for the curving vessel case, and $\beta = 2.3$ for the aneurysm case. As a result of this multiplication, the maximum intensity value in the image is beyond the maximum limit (255) for an 8-bit image. In order to render the intensity value within the range of 8-bit image (i.e. 0~255), a value of 80 was subtracted from the intensified image. The flow field simulated by CFD is interpolated in each pixel and used to generate the second image.

2.4.3 Image processing

Similar to the processing for particle images, appropriate Gaussian filter was applied to smoothen the intensity distribution. Then the smoothed image pair was used to estimate the velocity field using Equation (11) and (12). Another important technique employed in the present study is so-called “image-shift”, in which the first image is shifted towards the second image by using the discretized Equation (5) with the velocity field calculated from the DC-OFM. If the calculated velocity vector is greater than 1 pixel, the particular pixel will be shifted to a new coordinates in the image, according to the x- and y-component of the velocity vector. If the calculated velocity is less than 1 pixel, the intensity value at each pixel will be updated by calculation based on the calculated velocity in the previous step and the optical flow principle, i.e., by using discrete form of Equation (5). The new image with updated intensity distribution is treated as the shifted image for further analysis. The interested readers on image-shift technique are referred to the Liu and Shen [20]. Then, all steps mentioned above will be repeated to refine the flow field until the convergence criteria is met. For all cases in the present study, only one-time image-shift is quite enough to produce accurate flow field. The

velocity field calculated from the first step and second step (after image-shift) is merged to produce the final velocity results. The optical flow solver based on the DC-OFM for the DSA images is the same as the technique utilized in dealing with the particle images, including the image-shift technique. In fact, the application of Gaussian filter and image-shift technique partially accounts for the improvement of the accuracy for the present DC-OFM.

3. RESULTS AND DISCUSSIONS

3.1 Validation of the optical flow algorithm on particle images

Fig. 3 (a) shows the blurred particle image after smoothening twice by a Gaussian filter function ($s = 3$, $\sigma = 1.2$). Fig. 3 (b) shows the created particle image with the aforementioned Oseen vortex flow superimposed into the original image after a time step of $\Delta t = 0.02$ s, wherein the maximum displacement is about 0.5 pixel.

The flow velocities and streamlines are produced by the current OFM through analyzing the particle images and are presented in Fig. 4. Comparing the recovered results from the present method shown in Fig. 4 (a) and (c) to the exact velocity distribution in Fig. 4 (b) and (d), one can merely identify some differences in the high-speed region or called 'outer region' of the Oseen vortex. The error in velocity results is within 4% of the magnitude. Comparing the streamlines from the present method and the exact results shown in Fig. 4 (c) and (d), flow features of the Oseen vortices are recovered with adequate precision. Generally, the DC-OFM performed much better than the traditional Horn-Schunck method in producing an accurate velocity field. The error analysis indicates that the intensity gradient, and the time interval between the consecutive images, plays a key role in the accuracy of the OFM. In the OFM, the Lagrange multiplier is adjustable according to the needs of convergence. In the current case,

the Lagrange multipliers are selected as $\alpha_1 = 20$ in the Horn-Schunck method and $\alpha_2 = 2000$ in the present method, respectively. In fact, the Lagrange multiplier value in the Horn-Schunck method is pretty flexible (20~200) since it only serves as the initial input for the present method. The Lagrange multiplier for the current estimator within a range of 400~2000 has very little influence on the velocity profile except for the high speed region. Horn-Schunck estimator for $\alpha = 20$ and 2000 and the present algorithm ($\alpha_1 = 20$, $\alpha_2 = 2000$) were applied to the same particle image pair in order to make a point-by-point comparison. Velocity profiles were extracted at x = 128 pixels from the distribution and are prescribed in Fig. 5. Through comparison with the exact velocity profile, the present method underestimates the maximum velocity by about 4% in the outer region near to the vortex cores. In contrast to the present method, the velocity profile from the Horn-Schunck estimator features a very noisy fair for $\alpha = 20$. With an $\alpha = 2000$ used in the Horn-Schunck estimator, the results were significantly smoothed, nevertheless, it significantly underestimated the velocity magnitude in the whole region in comparing with the present method.

To further analyze the effect of the intensity gradient in the particle image on the error generation, the original particle image was smoothed by different mask size and standard deviation for the Gaussian function, which are presented in Fig. 6. Except for the last case, two Gaussian filter functions were applied to the image, where s_1 and s_2 represent the mask sizes, σ_1 and σ_2 represent the standard deviation for each Gaussian filter. Note that the particle image in Fig. 3 was smoothed by using two Gaussian filter functions with mask size and standard deviation of $s_1 = 3, \sigma_1 = 1.2$ and $s_2 = 3, \sigma_2 = 1.2$.The characteristic intensity gradient,γ, was defined as

$$\gamma = \frac{\sum_{i=1}^{n_x}\sum_{j=1}^{n_y}(E_x^2 + E_y^2)^{1/2}}{n_x n_y}. \quad (17)$$

where E_x, E_y represent the intensity gradient in x- and y- direction respectively, n_x and n_y represent the total pixel number in x- and y- direction respectively. This characteristic intensity gradient corresponds to the ∇E term in the error analysis. The intensity gradient was calculated by using a central discretization. The characteristic intensity gradient values corresponding to different mask size and standard deviation are summarized in Table 1. The autocorrelation radius was also calculated by using a plugin function, so called "Radially Averaged Autocorrelation", in Image J. The same velocity field was superimposed in each image to generate the second image, and then the velocity field was recovered by using the present OFM flow solver. The averaged errors in u and v component were calculated using Equation (18) and (19) and summarized in Table 1.

$$Error_u = \frac{\sum_{j=1}^{n_y}\sum_{i=1}^{n_x}|u - u_{exact}|}{n_{total}}, \quad (18)$$

$$Error_v = \frac{\sum_{j=1}^{n_y}\sum_{i=1}^{n_x}|v - v_{exact}|}{n_{total}}. \quad (19)$$

As presented in Fig. 6, obviously, the characteristic intensity gradient has a significant effect on the recovered velocity distributions. The lower intensity gradient was discovered to give rise to an increased deviation of the velocity from the exact solution. Moreover, the spatial fluctuation in the velocity profile was observed when the intensity gradient becomes very low with γ=2.9. Generally, better accuracy was obtained by increasing the characteristic intensity

gradient until the lowest error out of the five cases was observed for γ=13.4. Comparing the velocity results for γ=13.4 shown in Fig. 4(a), and for γ=17.2 shown in Fig. 6 (h), one can observe that the higher characteristic intensity gradient (γ=17.2) does not produce a better accuracy. This was also confirmed in the error analysis as shown in Table 1. It indicates that an optimum intensity gradient value exists for OFM estimation. It should be mentioned that the original particle image without smoothing cannot produce converged results.

Through adjusting the time interval between the pair of images for the case of $\gamma = 13.4$ from 0.2 s to 0.01 s, the effect of Δt is studies by comparing the error results. As presented in Fig. 7, the flow pattern was recovered well in each case, however, the overall velocity magnitude decreased obviously with the increase of time interval. The averaged errors in u and v component for each case are summarized in Table 2. The study on time interval (i.e. magnitude of displacement in image) demonstrated the error decreases with the reduced time interval, until the lowest error was observed at $\Delta t = 0.02$. The corresponding maximum displacement is about 0.5 pixel. For $\Delta t = 0.01$ s, the error is increased especially around the saddle points (i.e. the low speed region). This observation agrees well with the conclusion about time interval described in Liu and Shen [20].

3.2 Application of DC-OFM on DSA images of blood flow in vasculatures

3.2.1 CFD simulation of the blood flow in ICA and aneurysm

Fig. 8 (a) and (b) show the cropped DSA image with only ICA presented in the image, the configuration and mesh generated in the CFD software SC/Tetra corresponding to this case. Fig. 9 (a) and (b) present the aneurysm with a phantom artery added in the image and the CFD

mesh correspondingly. The total numbers of mesh for the ICA and aneurysm configuration are 6.7×10^5 and 5×10^5 respectively. The simulated flow field, which satisfied the aforementioned boundary conditions, are presented in Fig. 8 (c) and Fig. 9 (c), respectively. The SC/Tetra was well validated and used to conduct numerical study on the blood flow in cerebral aneurysm in our previous work [24]. In fact, the quantitative accuracy of the flow field, and the physical boundary condition at inlet and exit for the simulation is not a concern for the present study, because only a reasonable flow field is needed to create the second image for OFM analysis and comparison.

3.2.2 Application of DC-OFM on the blood flow in ICA

After the application of intensification with $\beta = 2.0$ on the original image in Fig. 10 (a), the image was output from the program and presented in Fig. 10 (b). The region outside of the artery was identified through detecting the boundary and the intensity value was set as fixed 255 (pure white) thus only the artery region is retained in the image. Through the intensification, the averaged intensity gradient, γ, was enhanced from 12.7 to 22.4. The simulated flow field was scaled up to make the maximum velocity reach about 50 pixel s^{-1}, and the time interval was set as $\Delta t = 0.01$ s, in order to make the maximum displacement in the image to be approximately 0.5 pixel. This arrangement leads to a better accuracy of the OFM as determined in the particle image study. The created image using Equation (1) after superimposing the flow field from CFD simulation is presented in Fig. 10 (c).

The image pair shown in Fig. 10 (b) and (c) is smoothed by applying a Gaussian filter (mask size of $s = 3$, standard deviation of $\sigma = 0.3$) to improve the smoothness of intensity distribution. The DC-OFM is applied to the smoothed image pair with $\alpha_1 = 20$ for the Horn-

Schunck flow solver (serving as the initial input for the present solver) and $\alpha_2 = 2000$ for the present flow solver. The "image-shift" technique was utilized to improve the accuracy of the calculated results. Fig. 11 (a) shows the exact velocity field generated from the CFD simulation. Fig. 11 (b) shows the velocity vectors recovered from the image pair shown in Fig. 10. The vectors in the plots were skipped by 2 in each direction to better present the velocity contour and flow feature. Essentially, the flow characteristics are recovered well as that the high speed regions, low speed regions and separation regions from the DC-OFM essentially match the exact velocity field. The velocity magnitude distribution is also matching the exact velocity. A map of the local error of the velocity magnitude defined as $|U(i,j) - U_{exact}(i,j)|$ is calculated and presented in Fig. 11 (c), where the subscript 'exact' denotes the CFD velocity distribution. One can observe that large errors appeared near the inlet, exit and the region near to the sharp turning region in the vessel. The velocity profiles at five cross sections at y=17 pixel, y=43 pixel, y=63 pixel, y=76 pixel and y=96 pixel (illustrated by dash lines in the figure) from CFD results and OFM results were plotted and compared in Fig. 11 (d). The agreement is acceptable, although the OFM results overshoot the exact velocity magnitude by nearly 20% nearer to the centerline, where the maximum velocity is generally located, at y=17 pixel, y=43 pixel and y=63 pixel. The overall averaged error in u-component and v-component are 3.5 pixel s^{-1} and 3.9 pixel s^{-1} respectively, which corresponds to 7.0% and 7.8% of the maximum velocity in the field. Through comparing the location of large error and poor intensity distribution, we observed that the region with the largest error is correlated with a poor intensity distribution to some extent, such as low brightness gradient, sharp change of intensity etc. In the region of very low or very high intensity gradient, the present optical flow algorithm tends to slightly underestimate the

velocity magnitude in most region; while in some particular region near the centerline of lumen as presented in Fig. 11, the present method tends to over predict the velocity magnitude.

In the inlet and outlet region of vessel, there is obvious error in the calculation of the velocity gradient and intensity gradient because of the lack of accurate information outside the image boundary. In studies of DSA images, the feature of isotropic distribution of intensity and relatively low-intensity value are not in favor of optical flow algorithms. The systematical error caused by a relatively low intensity gradient can be reduced by intensification. On the other hand, the sharpness of the intensity distribution can be smoothed by employing the Gaussian filter. Another important technique used in the present study was “image-shift”, which allowed a refinement after shifting and augmented the accuracy of the velocity estimation.

3.2.3 Application of DC-OFM on the flow in an intracranial aneurysm

Accurate measurements of the blood velocity distribution in the aneurysm is particularly important for the estimation of WSS and the analysis of the growth and rupture of aneurysm [25]. The method was further validated using the cropped image of an unruptured arterial aneurysm from the same patient, which represents another type of characteristic endovascular flow.

The DSA image from the same patient before coiling treatment is shown in Fig. 12 (a). The image was cropped to focus on the aneurysm sac shown in Fig. 12 (b). Then the image is intensified by a factor of $\beta = 2.3$ for the purpose of enhancing the sensitivity of the current OFM flow solver. Similar to the previous process, a value of 80 was subtracted to comply with the 8-bit image. Then the image was output from the program as presented in Fig. 12 (c). The intensification increased the characteristic intensity gradient from $\gamma = 5.1$ to $\gamma = 10.4$.

Similar to the previous case, the second image was generated by superimposing the simulated flow field from the CFD simulation. Then the image pair is smoothed by applying a Gaussian filter (mask size $s = 3$, standard deviation $\sigma = 0.6$) to improve the smoothness in the image. The DC-OFM is applied to the smoothed image pair with $\alpha_1 = 20$ for the Horn-Schunck flow solver and $\alpha_2 = 2000$ for the present flow solver. The "image-shift" technique was utilized to improve the accuracy of the calculation results. Fig. 13 (a) shows the velocity vectors recovered from the image pair using the present method. Fig. 13 (b) shows the velocity field generated from CFD simulation results. The vectors in the plots were skipped by 2 in each direction to better present the velocity contour and flow feature. It is noted that there is a region without velocity vectors because of the uniformly-distributed low intensity region (at inlet of the aneurysm) in the original image shown in Fig 12. Intensity gradient value in this region is almost zero, therefore the velocity cannot be resolved using OFM. One can observe that the flow pattern of a single vortex with the core of the vortex located at the center of the sac is recovered pretty well in comparison with the exact flow field. Both the high speed region near to the upper edge of sac, and low speed region near to the center in the OFM results can match the exact velocity field. A map of the local error of the velocity magnitude is shown in Fig. 13 (c). One can observe that the relative large errors appeared near to the neck of the aneurysm in an upper position where the blood stream enters the sac, and a lower position where the blood stream leaves the sac.

The velocity profiles for five cross sections at x=12 pixel, x=24 pixel, x=34 pixel, x=44 pixel and x=51 pixel (illuminated by dash line in the figure) from the exact and the recovered velocity distribution were plotted and compared in Fig. 13 (d). Similar profiles were observed at

each location although the OFM tends to over predict the velocity near to central region of the sac, at x=24 pixel and x=51 pixel. The overall averaged error in u-component and v-component is 3.1 pixel s^{-1} and 3.8 pixel s^{-1} respectively, which corresponds to 6.2% and 7.6% of the maximum velocity in the field.

It should be stated that the current method can only deal with a 2-D flow which is a projection of the 3-D blood flow on the image plane. If there is a strong out-of-plane velocity component involved in the projection, the accuracy of the current method would be vulnerable to this type of strong three-dimensional flow. The research on the accuracy of the present method in estimating flow with an out-of-plane component will be conducted in the future study. It also suggests that a smart choice of imaging to avoid large out-of-plane movement would be critical in estimating the blood velocity in both tortuous vessel and aneurysm. Varying path length gives rise to variation in contrast which could generate noise in the DSA image and thus lead to error in the velocity estimation. The present study cannot take into account this error, but it can be addressed in the future study for *in vivo* blood velocity estimation.

4. Conclusion and future direction

The DC-OFM developed in the present study is first validated and examined by using a particle image generated from a PIV test, and then applied to the DSA images for blood flow in ICA and aneurysm. Synthetic image pairs were generated by using a known flow field.

To conclude, the DC-OFM is promising and has demonstrated the ability to produce accurate and useful blood flow distributions in the vascular system. This could lead to key information, e.g., the WSS, for the diagnosis of and treatment planning for multiple vascular

diseases such as brain aneurysms. It also provides important flow details which can help verify the computational efforts on hemodynamics.

The error associated with the isotropic features added to the impact of a relative large time interval (i.e., low frame rate) between consecutive images, in fact, are main sources of error for the velocity estimation from *in-vivo* DSA images. The isotropic characteristics of intensity distribution in DSA image might be improved by using pulsatile injection of contrast medium during the DSA process, which could potentially produce a higher intensity gradient. Through comparing the results from the particle images and DSA images, we would suggest using safety-proof particles [22, 26] for DSA imaging might generate more accurate measurements of the blood velocity inside the vascular system. The requirement of short time interval is particularly challenging in the X-ray imaging process in biomedical applications. Most commercial X-ray imaging systems, such as the Siemens Artis Zee system used in the present study, have a maximum frame rate of about 15 Hz. X-ray systems with higher frame rates, e.g., 60 Hz and 150 Hz, were used to make measurements of blood flow rate with traditional OFM as is seen in the processing method [17, 19]. Although the maximum blood flow velocity in the vascular system is relatively low (in the order of ~1 m/s), it still requires a very high frame rate in order to generate the movement in the order of one pixel (required by the present OFM) in the image sequence. The particular requirement of displacement of 0.5 pixel frame^{-1}, which was determined as the best in the study of particle images, will drive the X-ray system to have a very high frame rate, e.g., 10,000 Hz. An alternative solution is to use a double-pulse X-ray system instead, in which the time delay between two pulses could be very short, e.g., in nanoseconds, and even adjustable to fit the request. Unfortunately, such a system is still not

available in the market yet. Therefore, a future direction for the development and greater application of OFM in the blood flow diagnosis relies on the development of such hardware. A high repetition rate X-ray system or a double-pulse X-ray system, with higher resolution, is required for accurate measurements of blood velocity distribution and hence WSS distribution.

ACKNOWLEDGEMENTS

The authors acknowledge the support from the Wright State University Translational Research Development Grants. The authors would like to thank Dr. Tianshu Liu in Western Michigan University for his help and suggestions on this paper.

Conflict of interest statement

There are no conflicts of interest that could inappropriately influence this research work.

REFERENCES

[1] Boersma, E., Mercado, N., Poldermans, D., Gardien, M., Vos, J., Simoons, M. L., 2003, "Acute Myocardial Infarction," Lancet, **361**(9360), pp. 847-858. DOI: 10.1016/S0140-6736(03)12712-2

[2] Brisman, J. L., Song, J. K., Newell, D. W., 2006, "Cerebral Aneurysms," N. Engl. J. Med., **355**, pp. 928-939. DOI: 10.1056/NEJMra052760

[3] Fouras, A., Kitchen, M. J., Dubsky, S., Lewis, R. A., Hooper, S. B., Hourigan, K., 2009, "The Past, Present, and Future of X-ray Technology for In Vivo Imaging of Function and Form," J. of Appl. Phys., **105**, 102009. DOI: 10.1063/1.3115643

[4] Malek, A. M., Alper, S. L., Izumo, S., 1999, "Hemodynamic Shear Stress and Its Role in Atherosclerosis," JAMA, **282**(21), pp. 2035-2042. DOI: 10.1001/jama.282.21.2035

[5] Jou, L. D., Lee, D. H., Morsi, H., Mawad, M. E., 2008, “Wall Shear Stress on Ruptured and Unruptured Intracranial Aneurysms at the Internal Carotid Artery,” AJNR Am. J. Neuroradiol., **29**, pp. 1761-1767. DOI: 10.3174/ajnr.A1180

[6] Xiang, J., Natarajan, S. K., Tremmel, M., Ma, D., Mocco, J., Hopkins, L. N., Levy, E. I., Meng, H., 2011, “Hemodynamic-morphologic Discriminants for Intracranial Aneurysm Rupture,” Stroke, **42**, pp. 144–152. DOI: 10.1161/STROKEAHA.110.592923

[7] Pereira, V. M., Ouared, R., Brian, O., Bonnefous, O., Satwiaski, J., Aerts, H., Ruijters, D., van Nijnatten, F., Perren, F., Bijlenga, P., Schaller, K., Lovblad, K. O., 2014, “Quantification of Internal Carotid Artery Flow with Digital Subtraction Angiography: Validation of An Optical Flow Approach with Doppler Ultrasound,” AJNR Am. J. Neuroradiol., **35**(1), pp. 156-163. DOI: 10.3174/ajnr.A3662

[8] Shpilfoygel, S., Close, R., Valentino, D., Duckwiler, G., 2000, “X-ray Vidiodensitometric Methods for Blood Flow and Velocity Measurement: A Critical Review of Literature,” Med. Phys., **27**, pp. 2008-2023. DOI: 10.1118/1.1288669

[9] Horn, B. K., Schunck, B.G., 1981, “Determining Optical Flow,” Artif. Intell., **17**, pp. 185-204. DOI: 10.1016/0004-3702(81)90024-2

[10] Corpetti, T., Memin, E., Perez, P., 2002, “Dense Estimation of Fluid Flows,” IEEE Trans. Patt. Anal. Mach. Intell., **24**(3), pp. 365-380. DOI: 10.1109/34.990137

[11] Corpetti, T., Heitz, D., Arroyo, G., Memin, E., Santa-Cruz, A., 2006, “Fluid Experimental Flow Estimation Based on An Optical Flow Scheme,” Exps. Fluids, **40**(1), pp. 80-97. DOI: 10.1007/s00348-005-0048-y

[12] Ruhnau, P., Kohlberger, T., Schnorr, C., Nobach, H., 2005, “Variational Optical Flow Estimation for Particle Image Velocimetry,” Exps. Fluids, **38**(21), pp. 21-32. DOI:10.1007/s00348-004-0880-5

[13] Yuan, J., Schnorr, C., Memin, E., 2007, “Discrete Orthogonal Decomposition and Variation Fluid Flow Estimation,” J. Math. Imaging Vision, **28**(1), pp. 67-80. DOI: 10.1007/s10851-007-0014-9

[14] Sarry, L., Boire, J. Y., Zanca, M., Lusson, J. R., Cassagnes, J., 1997, “Assessment of Stenosis Severity Using a Novel Method to Estimate Spatial and Temporal Variations of Blood Flow Velocity in Biplane Coronarography,” Phy. Med. Biol., **42**(8), pp. 1549-1564.

[15] Rhode, K., Lambrou, T., Hawkes, D., Seifalian, A., 2005, “Novel Approaches to the Measurement of Arterial Blood Flow from Dynamic Digital X-ray Images,” IEEE Trans. Med. Imaging, **24**(4), pp. 500-513. DOI: 10.1109/TMI.2004.843202

[16] Bonnefous, O., Pereira, V., Ouared, R., Rrina, O., Aerts, H., Hermans, R., Nijnatten, F., Stawiaski, J., and Ruijters, D., 2012, “Quantification of Arterial Flow Using Digital Subtraction Angiography,” Med. Phys., **39**, pp. 6264-6275. DOI: 10.1118/1.4754299

[17] Brina, O., Ouared, R., Bonnefous, O., van Nijnatten, F., Bouillot, P., Bijlenga, P., Schaller, K., Lovblad, K., Grunhagen, T., Ruijters, D., Pereira, V. 2014, “Intra-aneurysmal Flow Patterns: Illustrative Comparison Among Digital Subtraction Angiography, Optical Flow, and Computational Fluid Dynamics,” AJNR Am. J. Neuroradiol. DOI: 10.3174/ajnr.A4063

[18] Huang, T., Wu, T., Lin, Y., Guo, W., Huang, W., Lin, C., 2013, “Quantitative Flow Measurements by Digital Subtraction Angiography in Cerebral Carotid Stenosis Using Optical Flow Method,” J. X-ray Sci. Technol., **21**(2), pp. 227-235. DOI: 10.3233/XST-130373

[19] Pereira, V. M., Bonnefous, O., Ouared, R., Brina, O., Stawiaski, J., Aerts, H., Ruijters, D., Narata, A., Bijlenga, P., Schaller, K., Lovblad, K., 2013, "A DSA-based Method Using Contrast-motion Estimation for the Assessment of the Intra-aneurysmal Flow Changes Induced by Flow-diverter Stents," AJNR Am. J. Neuroradiol., **34**(4), pp. 808-815. DOI: 10.3174/ajnr.A3322

[20] Liu, T., Shen, L., 2008, "Fluid Flow and Optical Flow," J. Fluid Mech., **614**, pp. 253-291. DOI: 10.1017/S0022112008003273

[21] Liu T., Merat, A., Makhmalbaf, M., Fajardo, C., Merati, P, 2015, "Comparison Between Optical Flow and Cross-Correlation Methods for Extraction of Velocity Fields from Particle Images," Exp. Fluids, **56**(8), [166]. DOI: 10.1007/s00348-015-2036-1

[22] Park, H., Yeom, E., and Lee, S. J., 2016, "X-ray PIV Measurement of Blood Flow in Deep Vessels of a Rat: An in vivo Feasibility Study," Sci. Rep., **6**, 19194.

[23] Okamoto, K., Nishio, S., Saga, T., Kobayashi, T., 2000, "Standard Images for Particle-Image Velocimetry," Meas. Sci. Technol., **11**(6), pp. 685-691.

[24] Yang, Z., Yu, H., Huang, P. G., Schwieterman, R., Ludwig, B., 2015, "Computational Fluid Dynamic Simulation of Intracranial Aneurysms – Comparing Size and Shape," J. Coast. Life Med., **3**(3), pp. 245-252. DOI: 10.12980/JCLM.3.201514JCLM-2015-0004

[25] Meng, H., Tutino, V. M., Xiang, J., Siddiqui, A., 2014, "High WSS or low WSS? Complex Interactions of Hemodynamics with Intracranial Aneurysm Initiation, Growth, and Rupture: Toward a Unifying Hypothesis," AJNR Am. J. Neuroradiol., **35**(7), pp. 1254-1262. DOI: 10.3174/ajnr.A3558

[26] Vennemann, P., Lindken, R., and Westerweel, J., 2007, “In Vivo Whole-field Blood Velocity Measurement Techniques,” Exp. Fluids, **42**(4), pp.495-511.

NOMENCLATURE

A	area for integral
B	boundary term
c_f	scattering or absorption coefficient
D	diffusion coefficient
E	intensity on the image
E_{exact}	exact intensity value
$Error_u$	error in u component
$Error_v$	error in v component
f	source term
i	node number in x-direction
j	node number in y-direction
J	an arbitrary function
L	an integrand equation
n_x	total pixel number in x direction
n_y	total pixel number in y direction
n_{total}	total pixel number in the image
r	radial distance
r_a	autocorrelation radius
r_c	core radius of the Oseen vortex

s	mask size for Gaussian filter
t	time
u	x-component velocity
U	velocity magnitude
U_{exact}	exact velocity magnitue
u_θ	circumferential velocity due to Oseen vortex
v	y-component velocity
u_x	spatial derivative of u with respect to x
u_y	spatial derivative of u with respect to y
v_x	spatial derivative of v with respect to x
v_y	spatial derivative of v with respect to y
$\vec{v}$	velocity vector
$\vec{v}_{exact}$	exact velocity vector
$\vec{v}'$	derivative of velocity
x	coordinate in horizontal direction
y	coordinate in vertical direction
α	Lagrange multiplier
β	intensifier coefficient
ε	an arbitrary variable to form a function
γ	characteristic intensity gradient

σ	standard deviation for Gaussian function
Γ	boundary term for integration
ψ	general quantity
ω	vortex strength
∇	del operator
Δ	difference
Δt	time interval

Figure Captions List

Fig. 1 (a) DSA image of the cerebral arteries with a coiled aneurysm; (b) Cropped image focusing on a curving section of ICA.

Fig. 2 (a) Original DSA image containing an unruptured aneurysm; (b) Cropped image of the aneurysm with additional phantom parent arteries.

Fig. 3 (a) Filtered original PIV particle image with $\gamma = 13.4$, $\Delta t = 0.02s$; (b) Created particle image after superimposing the Oseen vortex with $\Delta t =$ 0.02 s.

Fig. 4 Map of the velocity distribution recovered from the particle image pair: (a) OFM results of velocity field for $\gamma = 13.4$, $\Delta t = 0.02s$; (b) Exact velocity field; (c) Streamlines of OFM results; (d) Exact streamlines.

Fig. 5 Comparison of the x-component of velocities across the vortex cores extracted from the velocity distribution using different methods.

Fig. 6 Smoothed particle images and corresponding velocity distribution results (a) image with mask size and standard deviation of $s_1 = 12, \sigma_1 = 4.8, s_2 = 5, \sigma_2 = 2.0$, and with $\gamma = 2.9$; (b) velocity results corresponding to case (a); (c) image with mask size and standard deviation of $s_1 = 8, \sigma_1 = 3.2, s_2 = 3, \sigma_2 = 1.2$ with $\gamma = 6.1$; (d) velocity results corresponding to case (c); (e) image with mask size and standard deviation of $s_1 = 5, \sigma_1 = 2.0, s_2 = 3, \sigma_2 = 1.2$ with $\gamma = 9.3$; (f) velocity results corresponding to case (e); (g) image with mask size and standard deviation of $s_1 = 3, \sigma_1 = 1.2$ with $\gamma = 17.2$; (h) velocity results corresponding to case (g).

Fig. 7 Velocity results for image pairs generated by varied time interval with a fixed $\gamma = 13.4$: (a) Δt=0.2 s; (b) Δt=0.1 s; (c) Δt=0.05 s; (d) Δt=0.01 s.

Fig. 8 (a) Cropped DSA image focusing on the ICA; (b) CFD mesh for blood flow simulation; (c) CFD simulation results of the flow field used for generating the synthetic image.

Fig. 9 (a) Cropped DSA image focusing on the aneurysm (black lines were added to generate the phantom artery boundary to enable the CFD simulation); (b) CFD mesh; (c) CFD simulation results of the flow field.

Fig. 10 (a) Cropped DSA image of the curving ICA; (b) smoothed intensified image; (c) the second image generated by superimposing the flow field into the image (b).

Fig. 11 (a) Exact velocity distribution from CFD; (b) Recovered velocity using the present DC-OFM method; (c) Error distribution of velocity magnitude; (d) Velocity profile comparison at five cross sections.

Fig. 12 (a) DSA image of the cerebral arteries with an uncoiled aneurysm; (b) Cropped image focusing on the aneurysm; (c) Intensified aneurysm image ($\beta = 2.3$).

Fig. 13 (a) Exact velocity distribution in the aneurysm from CFD; (b) Recovered velocity distribution by using DC-OFM (c) Error distribution of velocity magnitude; (d) Comparison of velocity profiles at five cross sections.

Table Caption List

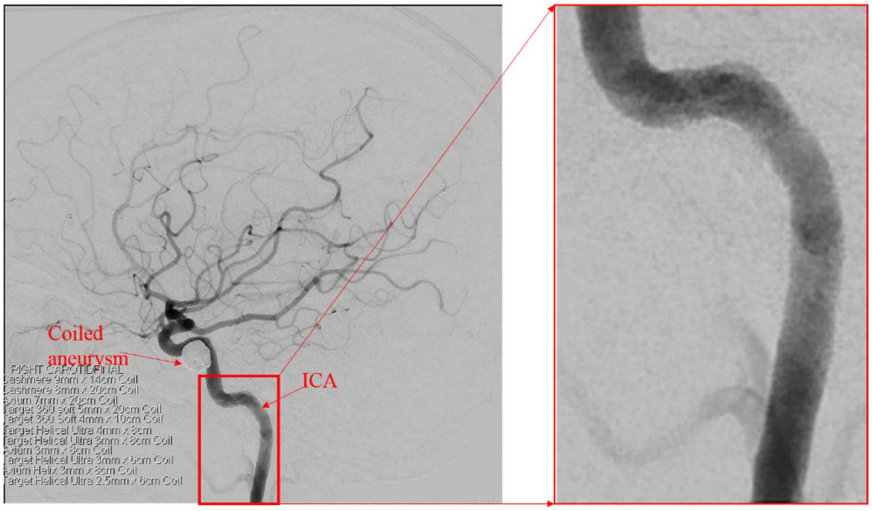

(a) (b)

Fig. 1 (a) DSA image of the cerebral arteries with a coiled aneurysm; (b) Cropped image focusing on a curving section of ICA.

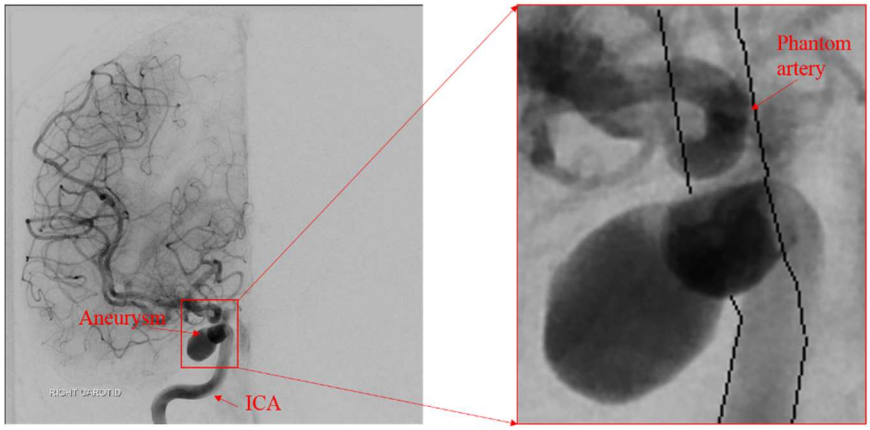

(a) (b)

Fig. 2 (a) Original DSA image containing an unruptured aneurysm; (b) Cropped image of the aneurysm with additional phantom parent arteries.

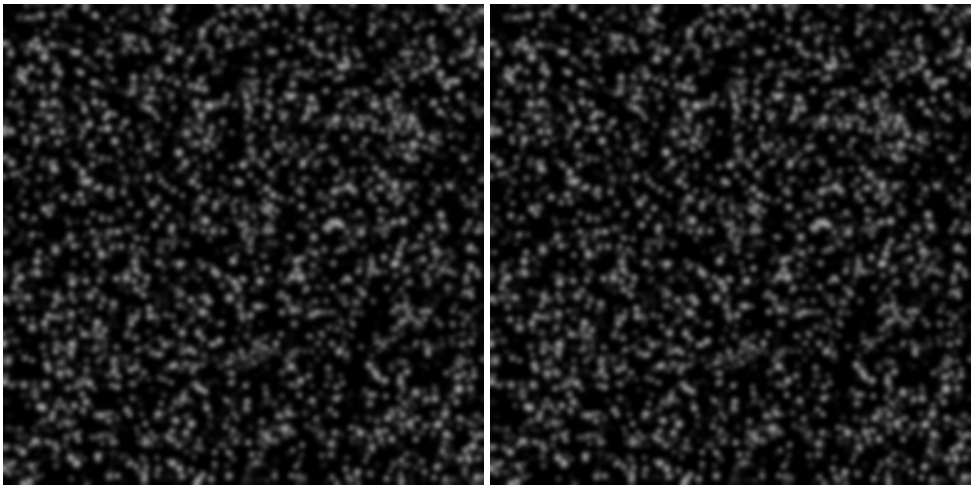

(a) (b)

Fig. 3 (a) Filtered original PIV particle image with $\gamma = 13.4$, $\Delta t = 0.02s$; (b) Created particle image after superimposing the Oseen vortex with $\Delta t = 0.02$ s.

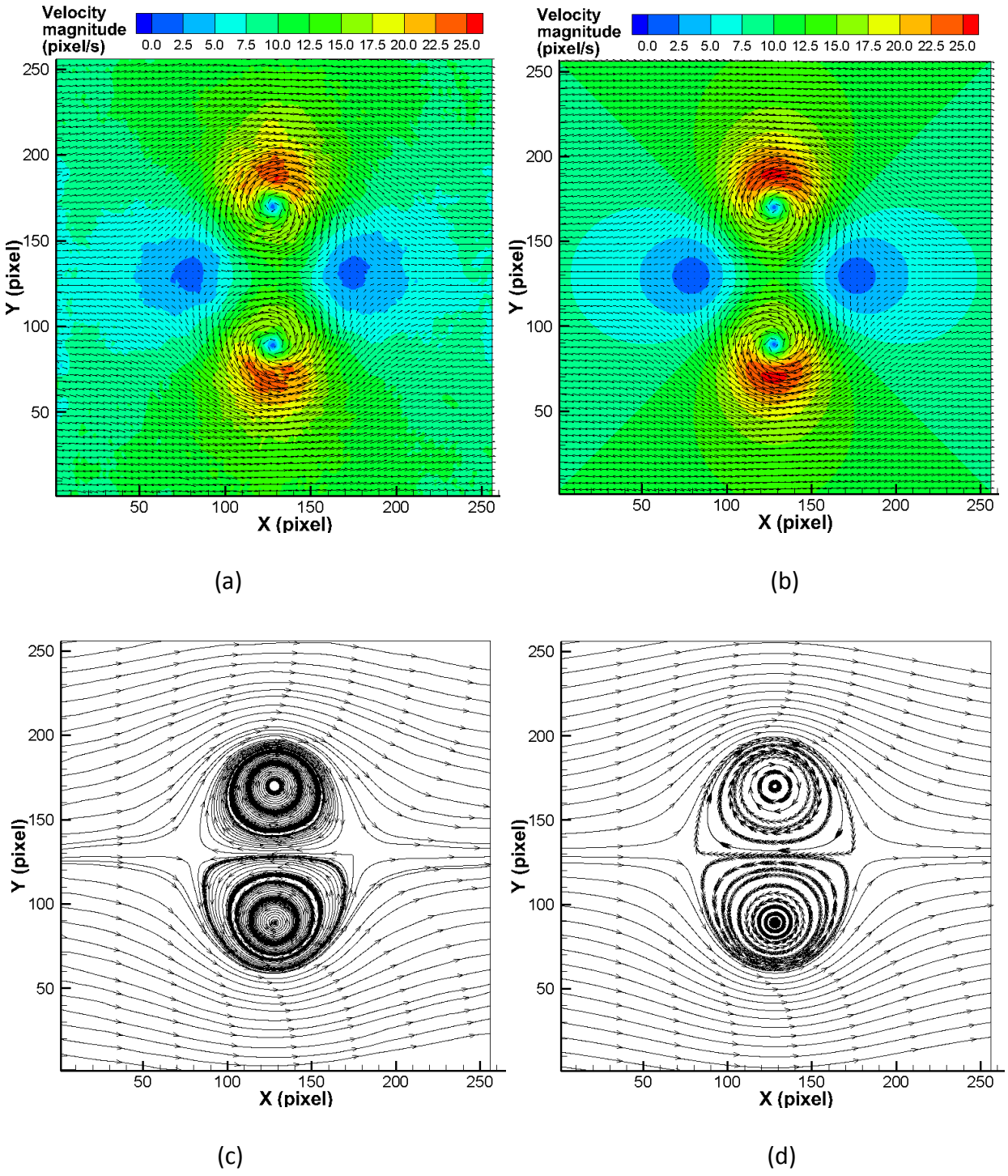

Fig. 4 Map of the velocity distribution recovered from the particle image pair: (a) OFM results of velocity field for $\gamma = 13.4$, $\Delta t = 0.02s$; (b) Exact velocity field; (c) Streamlines of OFM results; (d) Exact streamlines.

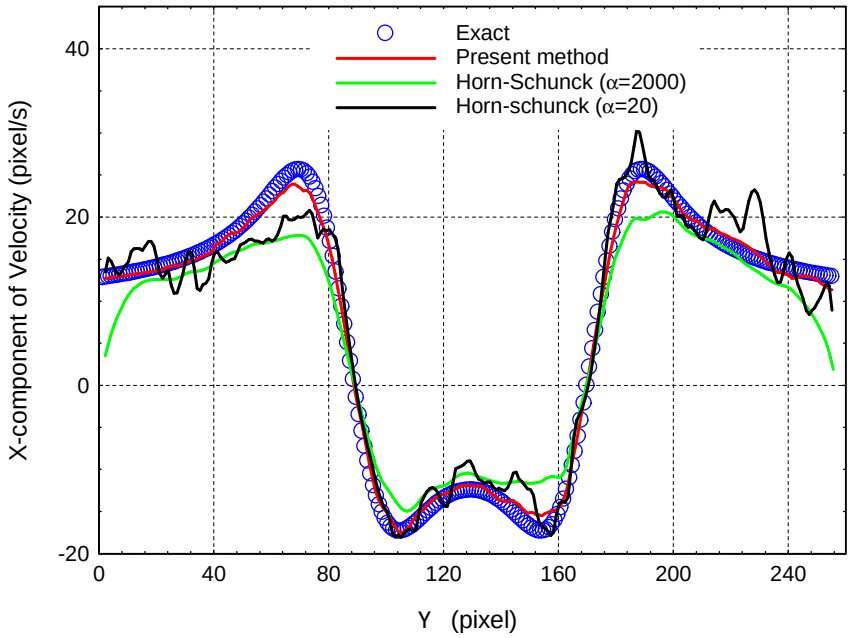

Fig. 5 Comparison of the x-component of velocities across the vortex cores extracted from the velocity distribution using different methods.

(a)

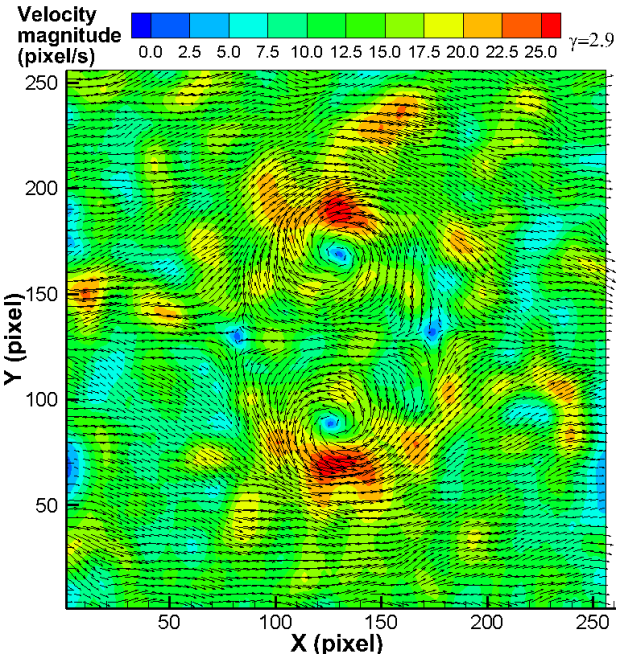
Velocity magnitude (pixel/s)
0.0 2.5 5.0 7.5 10.0 12.5 15.0 17.5 20.0 22.5 25.0
γ=2.9
250
200
150
100
50
Y (pixel)
50 100 150 200 250
X (pixel)

(b)

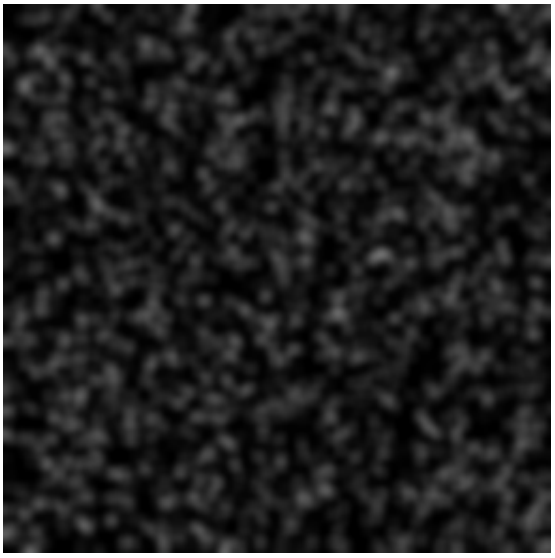

(c)

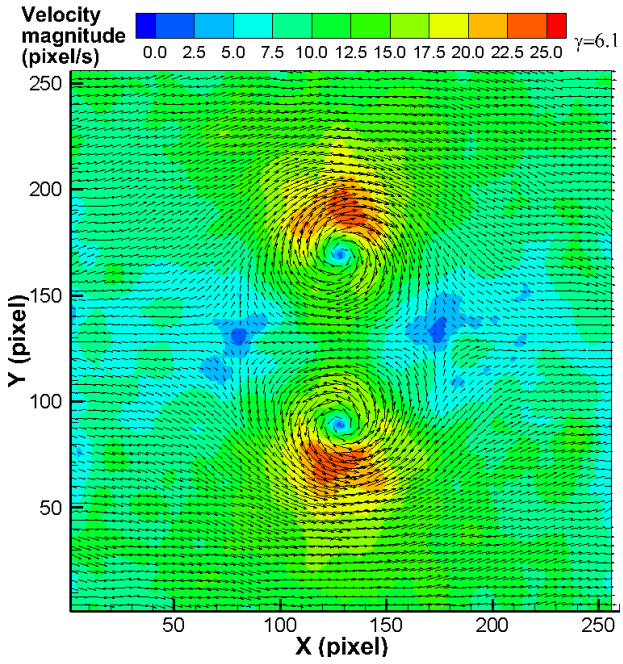
Velocity magnitude (pixel/s)
0.0 2.5 5.0 7.5 10.0 12.5 15.0 17.5 20.0 22.5 25.0
γ=6.1
250
200
150
100
50
Y (pixel)
50 100 150 200 250
X (pixel)

(d)

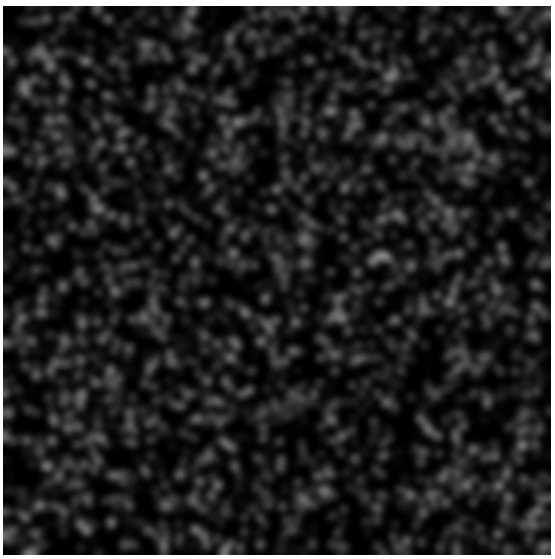

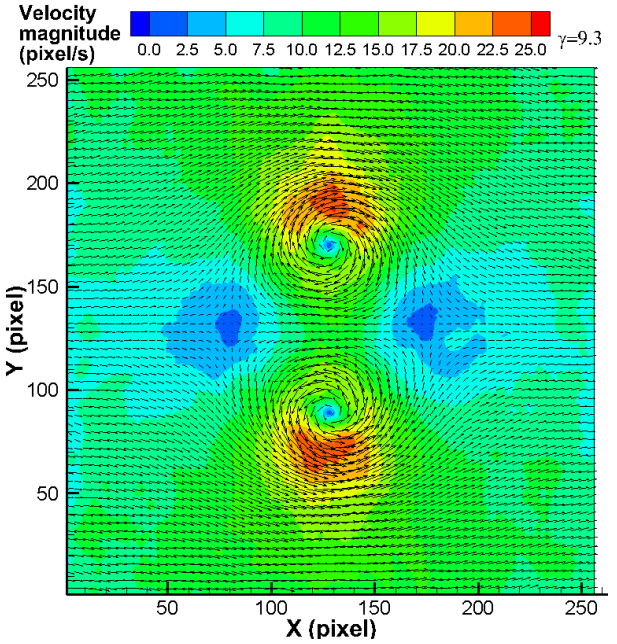

(e) (f)

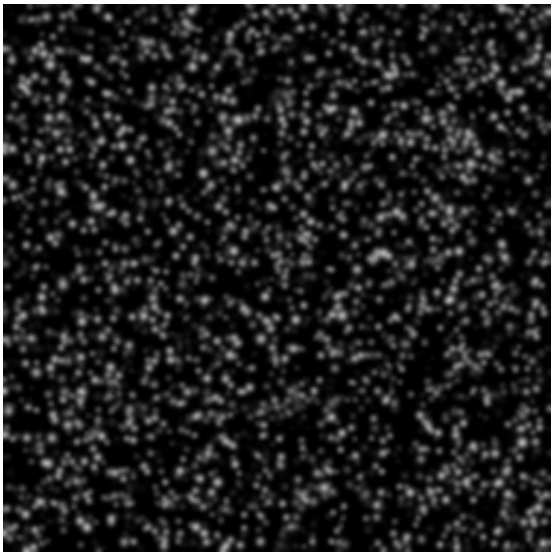

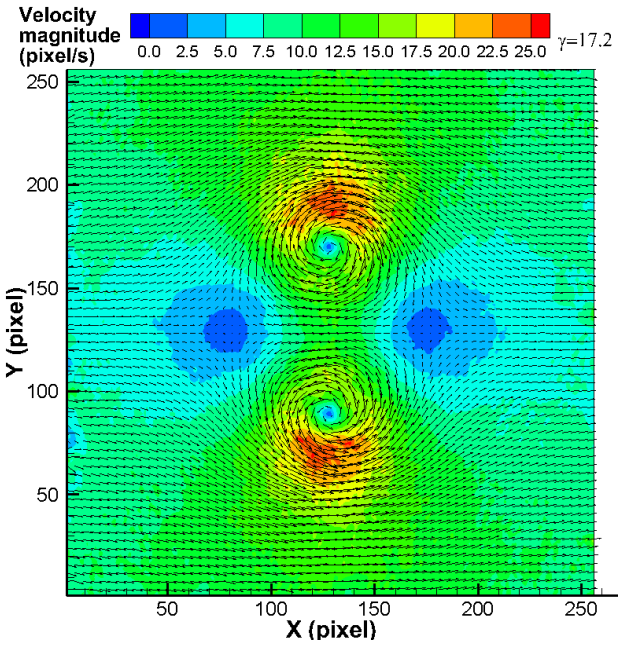

(g) (h)

Fig. 6 Smoothed particle images and corresponding velocity distribution results (a) image with mask size and standard deviation of $s_1 = 12, \sigma_1 = 4.8, s_2 = 5, \sigma_2 = 2.0$, and with $\gamma = 2.9$; (b) velocity results corresponding to case (a); (c) image with mask size and standard deviation of $s_1 = 8, \sigma_1 = 3.2, s_2 = 3, \sigma_2 = 1.2$ with $\gamma = 6.1$; (d) velocity results corresponding to case (c); (e)

image with mask size and standard deviation of $s_1 = 5, \sigma_1 = 2.0, s_2 = 3, \sigma_2 = 1.2$ with $\gamma = 9.3$; (f) velocity results corresponding to case (e); (g) image with mask size and standard deviation of $s_1 = 3, \sigma_1 = 1.2$ with $\gamma = 17.2$; (h) velocity results corresponding to case (g).

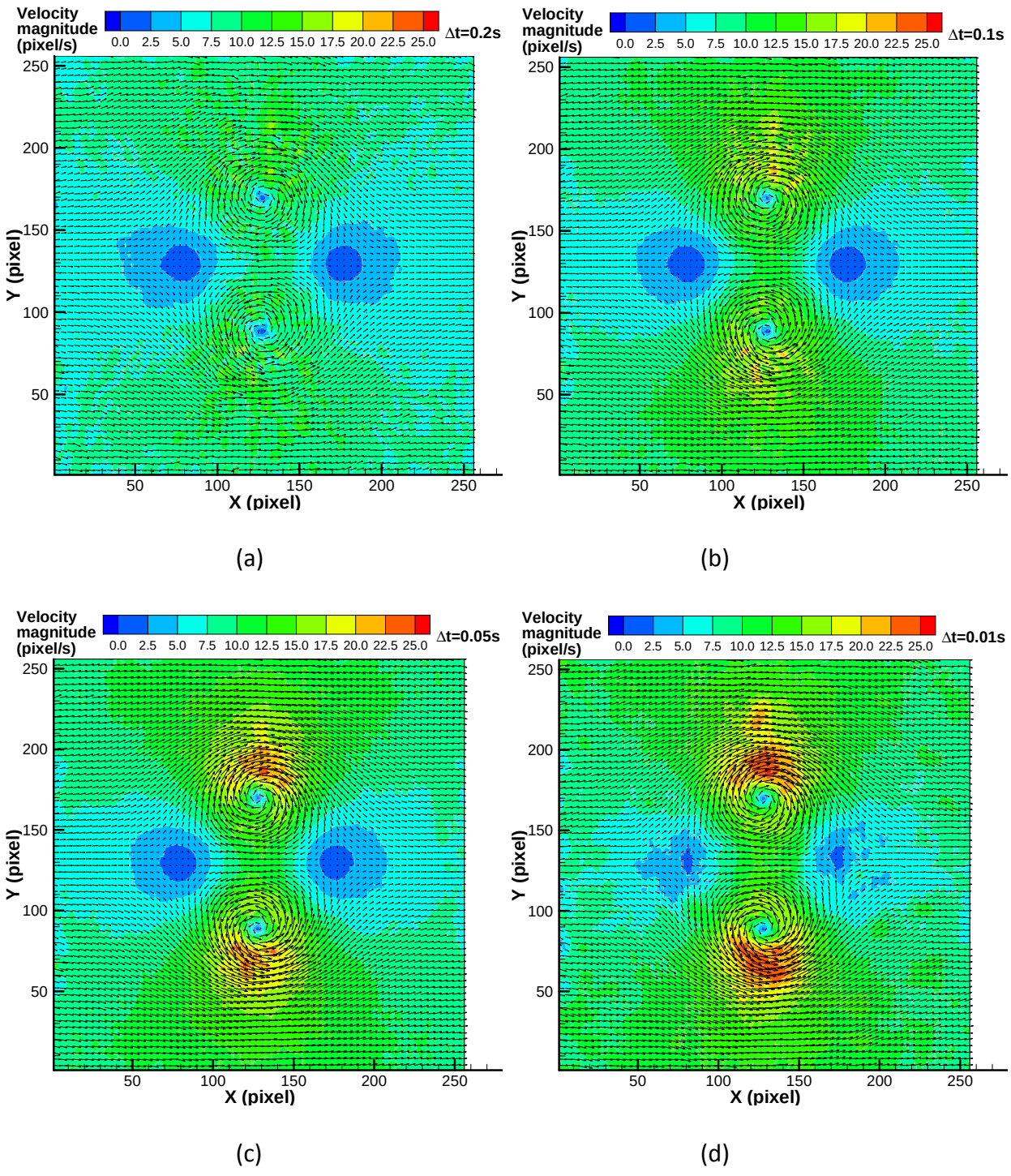

Fig. 7 Velocity results for image pairs generated by varied time interval with a fixed $\gamma = 13.4$: (a) Δt=0.2 s; (b) Δt=0.1 s; (c) Δt=0.05 s; (d) Δt=0.01 s.

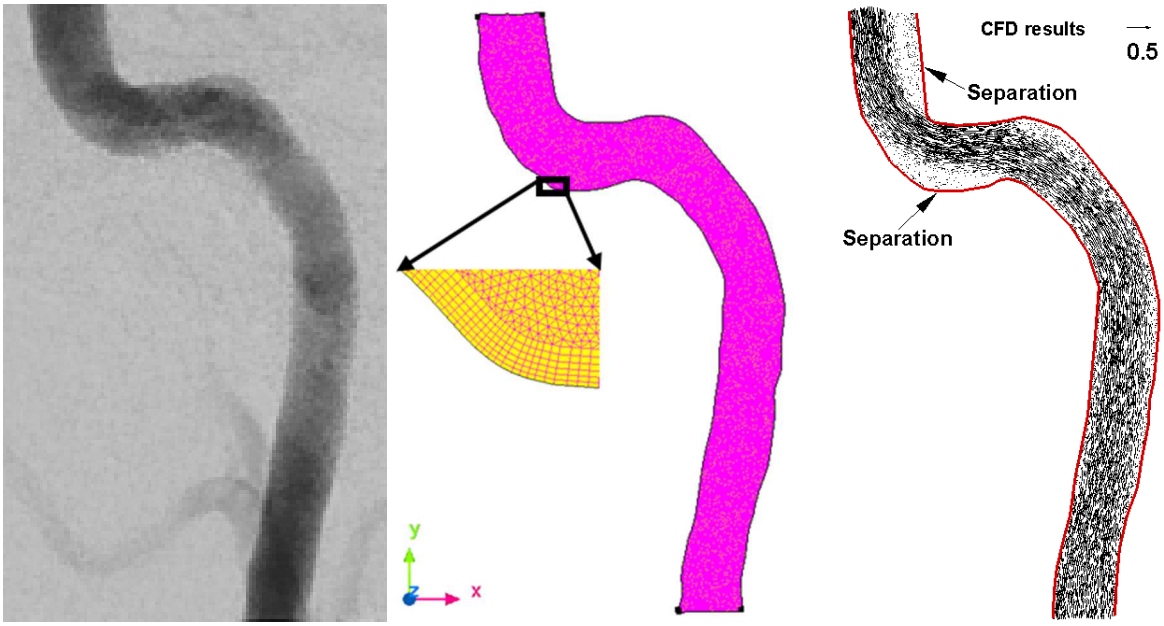

(a) (b) (c)

Fig. 8 (a) Cropped DSA image focusing on the ICA; (b) CFD mesh for blood flow simulation; (c) CFD simulation results of the flow field used for generating the synthetic image.

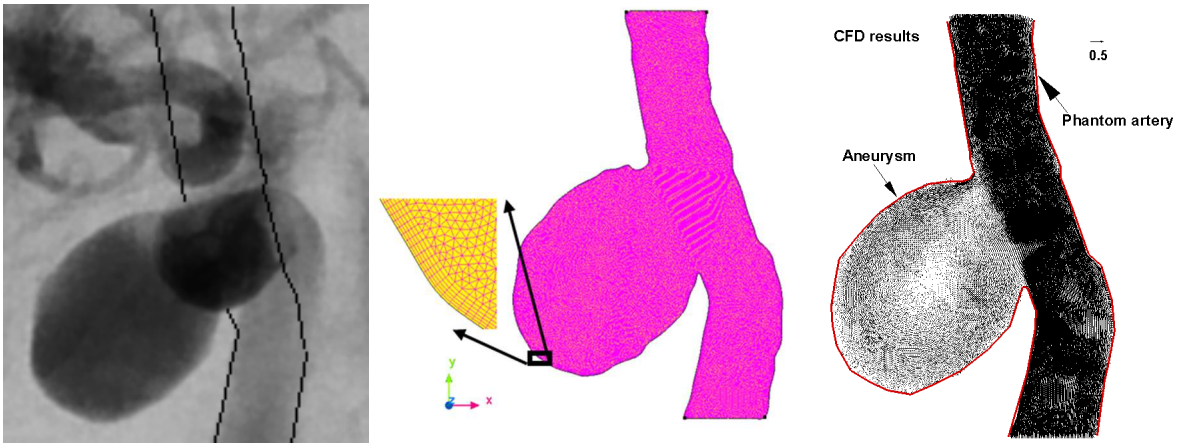

(a) (b) (c)

Fig. 9 (a) Cropped DSA image focusing on the aneurysm (black lines were added to generate the phantom artery boundary to enable the CFD simulation); (b) CFD mesh; (c) CFD simulation results of the flow field.

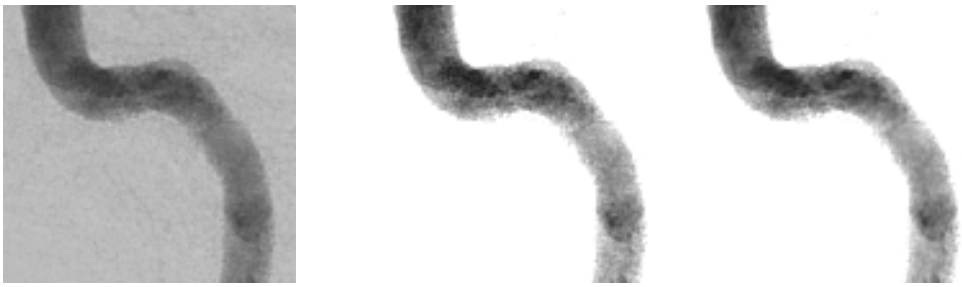

(a) (b) (c)

Fig. 10 (a) Cropped DSA image of the curving ICA; (b) smoothed intensified image; (c) the second image generated by superimposing the flow field into the image (b).

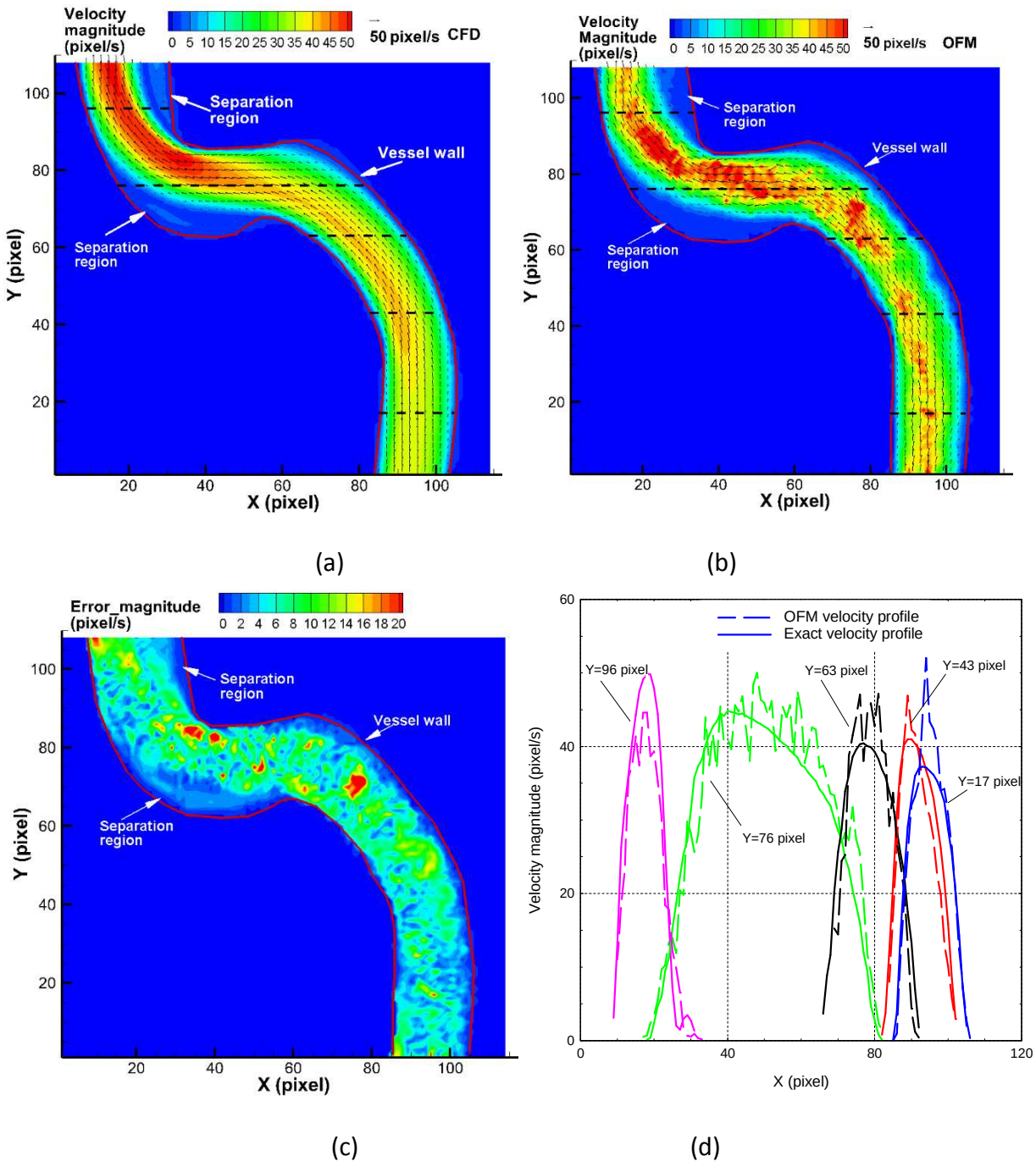

Fig. 11 (a) Exact velocity distribution from CFD; (b) Recovered velocity using the present DC-OFM method; (c) Error distribution; (d) Velocity profile comparison at five cross sections.

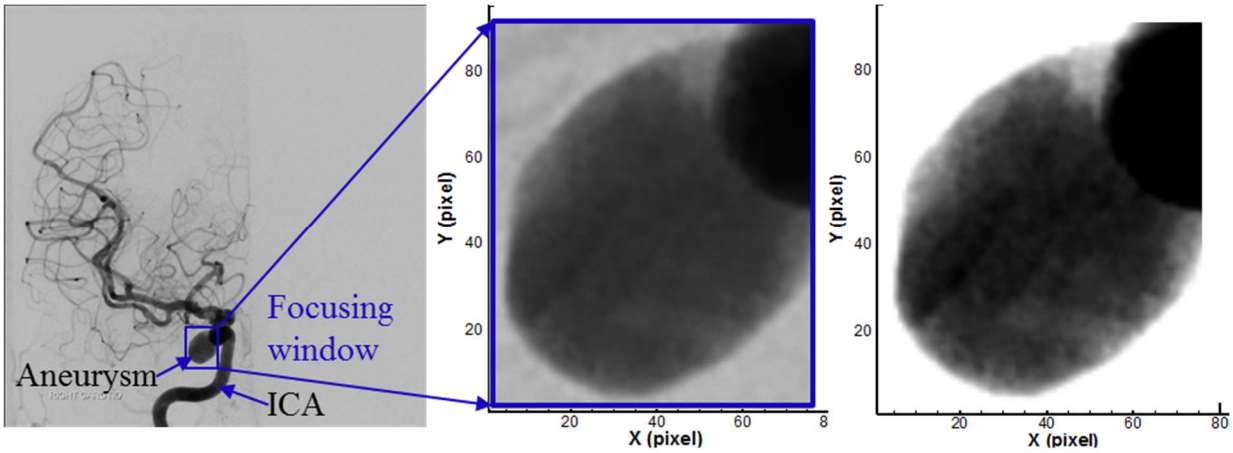

(a) (b) (c)

Fig. 12 (a) DSA image of the cerebral arteries with an uncoiled aneurysm; (b) Cropped image focusing on the aneurysm; (c) Intensified aneurysm image ($\beta = 2.3$).

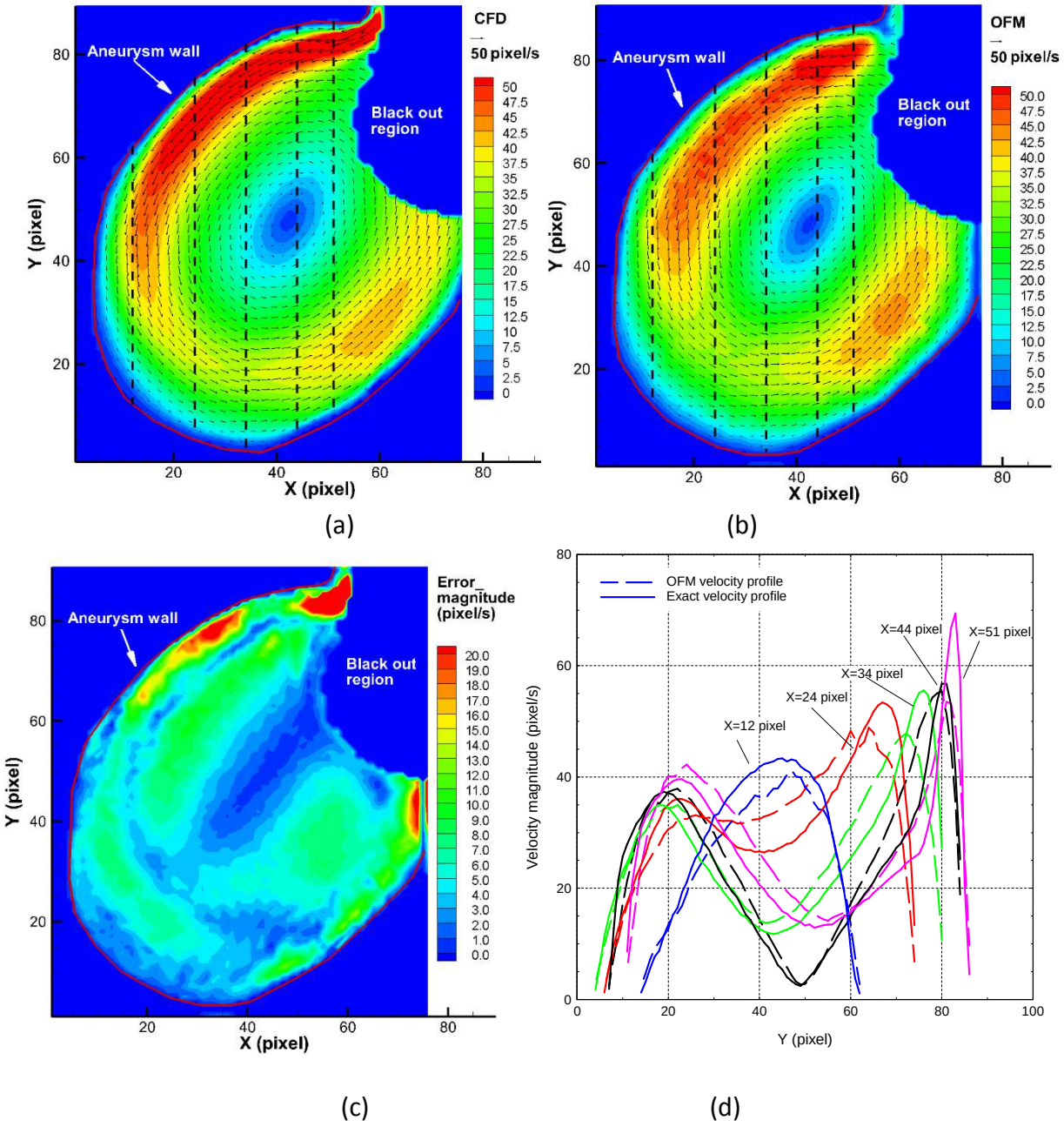

Fig. 13 (a) Exact velocity distribution in the aneurysm from CFD; (b) Recovered velocity distribution by using DC-OFM (c) Error distribution of velocity magnitude; (d) Comparison of velocity profiles at five cross sections.

Table 1 Averaged error for different intensity gradient

Intensity gradient γ (intensity pixel^{-1})	2.9	6.1	9.3	13.4	17.2
s_1 (pixel)	12	8	5	3	3
σ_1 (pixel)	4.8	3.2	2.0	1.2	1.2
s_2 (pixel)	5	3	3	3	N/A
σ_2 (pixel)	2.0	1.2	1.2	1.2	N/A
Autocorrelation Radius r_a (pixel)	12.6	9.1	8.0	7.4	6.7
$Error_u$ (pixel s^{-1})	2.90	0.87	0.48	0.43	0.51
$Error_v$ (pixel s^{-1})	2.40	0.73	0.40	0.33	0.37

Table 2 Averaged error for different time interval

Time interval Δt (s)	0.01	0.02	0.05	0.1	0.2
Averaged error in *u* (pixel s^{-1})	0.63	0.43	0.54	1.09	2.56
Averaged error in *v* (pixel s^{-1})	0.54	0.33	0.34	0.59	1.18